J Fusion Energ (2014) 33:319–335
DOI 10.1007/s10894-014-9683-8

REVIEW ARTICLE

Plasma Focus Radiative Model: Review of the Lee Model Code

S. Lee

Published online: 4 March 2014

Abstract The code couples the electrical circuit with plasma focus (PF) dynamics, thermodynamics and radiation. It is energy-, charge- and mass-consistent and accounts for the effects of transit times of small disturbances and plasma self-absorption. It has been used in design and interpretation of Mather-type PF experiments and as a complementary facility to provide diagnostic reference numbers in all gases. Information computed includes axial and radial dynamics, SXR emission characteristics and yield for various applications including microelectronics lithography and optimization of machines. Plasma focus neutron yield calculations, current and neutron yield limitations, deterioration of neutron scaling (neutron saturation), radiative collapse, speed-enhanced PF, current-stepped PF and extraction of diagnostic and anomalous resistance data from current signals have been studied using the code; which also produces reference numbers for fluence, flux and energy of deuteron beams and ion beams for all gases. There has been no pause in its continuous evolution in three decades so much so that the model code has no formal source reference except www.plasmafocus.net. This review presents, for the first time a comprehensive up-to-date version of the 5-phase model code. The equations of each phase are derived. Those of the first two phases are normalized to reveal important scaling parameters. The focus pinch phase is discussed with radiation-coupled dynamics necessitating the computation of radiation terms moderated by plasma self-absorption. Neutron and ion beam yields are computed. The 5-phase model code appears to be adequate for all Mather-type PF, lacking only in one aspect that for high inductance PF (termed Type 2) the measured current waveform contains an extended dip which cannot be fitted by the 5-phase code; necessitating an extended 6-phase code. This sixth phase (termed phase 4a) is dominated by anomalous resistance, providing a way to extract valuable data on anomalous resistivity from the current trace.

Keywords Plasma focus · Plasma focus modeling · Plasma focus radiation · Lee model code

S. Lee (✉)
Institute for Plasma Focus Studies, 32 Oakpark Drive, Chadstone 3148, Australia
e-mail: leesing@optusnet.com.au; leesing111@yahoo.com

S. Lee
INTI International University, 71800 Nilai, Malaysia

S. Lee
University of Malaya, 50603 Kuala Lumpur, Malaysia

Introduction

In the early 1960's, Filippov [1] and Mather [2] independently invented the plasma focus (PF) and carried out ground-breaking research establishing the Filippov- and Mather-type devices. In 1971, D. Potter published his Numerical Studies of the PF, a two-dimensional fluid model which estimated neutron yield concurring with experimental yields, and concluded that these neutrons were the result of thermally reacting deuterons in the hot pinch region [3]. Since then some five decades of research have been conducted computing and measuring all aspects of the PF [4–6], imaging for dynamics, interferometry for densities, spectroscopy for temperatures, measurements on neutrons and radiation yields, and MeV particles. The result is the commonly accepted picture today that mechanisms within the focus pinch, such as micro- and MHD instabilities, acceleration by turbulence and 'anomalous'

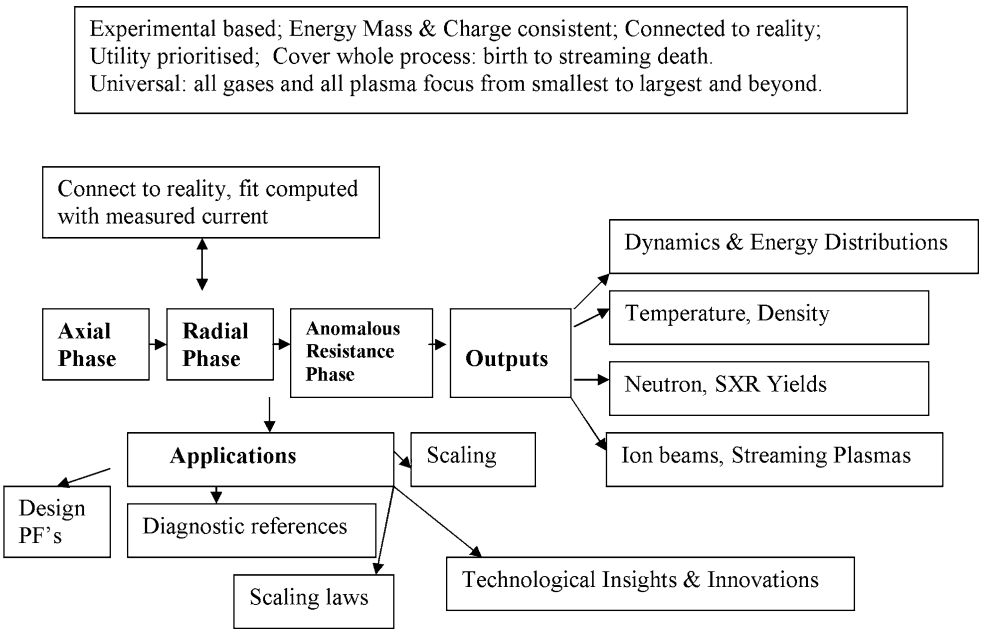

Fig. 1 The philosophy, the phases, the outputs and applications of the Lee model code

plasma resistance are important to PF behavior and that emitted neutrons do not originate from thermonuclear reactions.

In conjunction with the development of the PF known as the UNU/ICTP PFF [7] during the UNU Training Programme in Plasma and Laser Technology in 1985 [7–9] a 2-phase code had been developed [10, 11] to describe and optimize the design of the PF. The code [12] couples the electrical circuit with PF dynamics, thermodynamics and radiation. It is energy-, charge- and mass-consistent. It was used in the design and interpretation of experiments [7, 13, 14]. An improved 5-phase code [12] incorporating finite small disturbance speed [15], radiation and radiation-coupled dynamics was used [16–18], and was first web-published [19] in 2000. Plasma self-absorption was included [12, 19] in 2007. It has been used extensively as a complementary facility in several machines, for example: UNU/ICTP PFF [7, 14, 16–18], NX2 [18, 20], NX1 [18], DENA [21]. It has also been used in other machines for design and interpretation including sub-kJ PF machines [22], FNII [23], the UBA hard X-ray source [24], KSU PF [25] and a cascading PF [26]. Information computed includes axial and radial dynamics [7, 13, 14, 16, 17, 25], SXR emission characteristics and yield [17–20, 27–33] for various applications including as a source for microelectronics lithography [18], optimization of machines [7, 12, 16–20, 28] and adaptation in the form of ML (Modified Lee) to Filippov-type PF devices [21]. Speed-enhanced PF [16] was demonstrated. Plasma focus neutron yield calculations [34, 35], current and neutron yield limitations [36, 37], deterioration of neutron scaling (neutron saturation) [38, 39], radiative collapse [40], current-stepped PF [41], extraction of diagnostic data [33, 42–46] and anomalous resistance data [47–49] from current signals have been studied using the code [12] or variants. It has recently been used to produce reference numbers for deuteron beam number and energy fluence and flux and scaling trends for these with PF storage energy; and subsequently extended for beam ion calculations for all gases [50, 51]. Radiation and particle yields scaling laws [30, 32, 34, 38, 39, 50–55] have been deduced. The range and scope of this model code is shown in Fig. 1.

The continuing development of the code over the past 3 decades is the reason that no pause has been made to publish the basis and details of the model code; although in recent years many details, as they evolve, are described in the website of the Institute for Plasma Focus Studies [12]. This present review sets out to present the first complete description of the model code in its basic 5-phase version. The paper also briefly describes the development into the 6-phase version for Type-2 (high inductance PF) machines which have been found to be incompletely fitted with the 5-phase model due to a dominant anomalous resistance phase [47].

This model has been developed for Mather-type [2] PF machines. It was developed for the 3 kJ machine known as the UNU/ICTP PFF [7, 8] (United Nations University/ International Centre for Theoretical Physics Plasma Focus facility), which now forms an international network. However it has since been generalized to all machines. In principal there is no limit to energy storage and electrode configuration, though house-keeping may need to be carried out in extreme cases, in order to keep within efficient ranges e.g. of graph plotting.

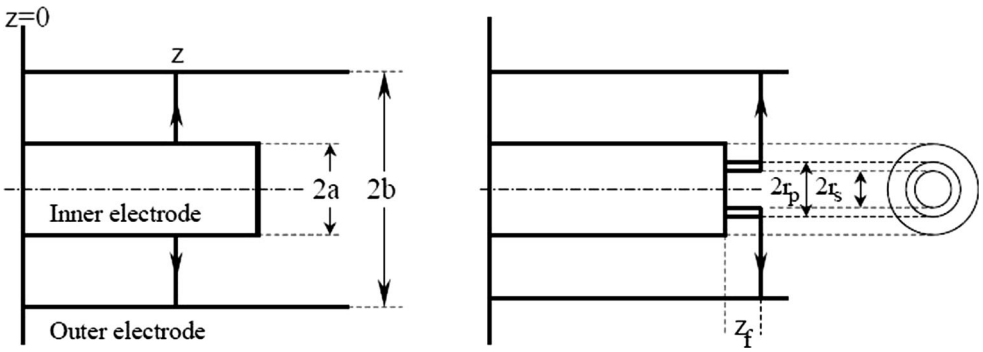

Fig. 2 Schematic of the axial and radial phases. *Left* **a** depicts the axial phase; *right* **b** the radial phase. In **a**, z is the effective position of the current sheath-shock front structure. In **b** r_s is the position of the inward moving shock front driven by the piston at position r_p. Between r_s and r_p is the radially imploding slug, elongating with a length z_f

The Five Phases of the Plasma Focus

A brief description of the five phases is summarised as follows (see Fig. 2):

1. Axial phase: This is described by a snowplow model with an equation of motion which is coupled to a circuit equation. The equation of motion incorporates the axial phase model parameters: mass and current factors f_m and f_c [13, 56–58]. The mass swept-up factor f_m accounts for not only the porosity of the current sheet but also for the inclination of the moving current sheet-shock front structure and all other unspecified effects which have effects equivalent to increasing or reducing the amount of mass in the moving structure, during the axial phase. The current factor, f_c, accounts for the fraction of current effectively flowing in the moving structure (due to all effects such as current shedding at or near the back-wall, current sheet inclination). This defines the fraction of current effectively driving the structure, during the axial phase.
2. Radial inward shock phase (see Figs. 2, 4): Described by four coupled equations using an elongating slug model. The first equation computes the radial inward shock speed from the driving magnetic pressure. The second equation computes the axial elongation speed of the column. The third equation computes the speed of the current sheath (CS), also called the magnetic piston, allowing the current sheath to separate from the shock front by applying an adiabatic approximation. The fourth is the circuit equation. Thermodynamic effects due to ionization and excitation are incorporated into these equations (as well as for all radial phases), these effects being important for gases other than hydrogen and deuterium. Temperature and number densities are computed during this phase. A communication delay between shock front and current sheath due to the finite small disturbance speed is crucially implemented in this phase. The model parameters, radial phase mass swept-up and current factors, f_{mr} and f_{cr}, are incorporated in all three radial phases. The mass swept-up factor f_{mr} accounts for all mechanisms which have effects equivalent to increasing or reducing the amount of mass in the moving slug, during the radial phase. The current factor, f_{cr}, accounts for the fraction of current effectively flowing in the moving piston forming the back of the slug (due to all effects). This defines the fraction of current effectively driving the radial slug.
3. Radial reflected shock (RS) phase: When the shock front hits the axis, because the focus plasma is collisional, a reflected shock RS develops which moves radially outwards, whilst the radial current sheath (CS) piston continues to move inwards. Four coupled equations are also used to describe this phase, these being for the RS moving radially outwards, the piston moving radially inwards, the elongation of the annular column and the circuit. The same model parameters, f_{mr} and f_{cr}, are used as in the previous radial phase. The plasma temperature behind the RS undergoes a jump by a factor nearly 2.
4. Slow compression (Quiescent) or pinch phase: When the out-going RS hits the in-coming piston the compression enters a radiative phase in which for gases such as neon, argon, krypton and xenon, radiation emission may actually enhance the compression where we have included energy loss/gain terms from Joule heating and radiation losses into the piston equation of motion. Three coupled equations describe this phase; these being the piston radial motion equation, the pinch column elongation equation and the circuit equation, incorporating the same model parameters as in the previous two phases. Thermodynamic effects [59] are incorporated into this phase. Radiation yields are computed incorporating the effects of plasma self-absorption. Thermonuclear and beam-gas target components of neutron yields are computed as are properties of fast ion beams (FIB) and fast plasma streams (FPS) exiting the focus pinch. The duration of this slow compression phase is set as the

time of transit of small disturbances across the pinched plasma column. The computation of this phase is terminated at the end of this duration.

5. Expanded column phase: To simulate the current trace beyond this point, we allow the column to suddenly attain the radius of the anode, and use the expanded column inductance for further integration. In this final phase the snowplow model is used, and two coupled equations are used; similar to the axial phase above. This phase is not considered important as it occurs after the focus pinch.

We note that the transition from Phase 4 to 5 is observed in laboratory measurements to occur in an extremely short time with plasma/current disruptions resulting in localized regions of high densities and temperatures. These localized regions are not modeled in the code, which consequently computes only an average uniform density, and an average uniform temperature which are considerably lower than measured peak density and temperature. We have investigated profiling techniques to estimate these peaks [60]. However, because the 4 model parameters are obtained by fitting the computed total current waveform to the measured total current waveform, the model incorporates the energy and mass balances equivalent, at least in the gross sense, to all the processes which are not even specifically modeled. Hence the computed gross features such as speeds and trajectories and integrated soft X-ray yields have been extensively tested in numerical experiments for many machines across the range of machines and are found to be comparable with measured values. The statements in this paragraph apply to both Type-1 (low inductance) and Type-2 (high inductance) PF machines [47]. However it has been found that whilst Type-1 current waveforms can be fitted adequately with the 5-phase code, the current waveform of a Type-2 machine typically contains current dip with a first portion that is well-fitted by the 5-phase code. Beyond the first portion of the dip there is an extended dip which cannot be fitted by the 5-phase model however much the model parameters are stretched. Therefore for Type-2 machines an additional sixth phase (termed Phase 4a) has been coded occurring between Phase 4 and 5 above which is fitted by assuming anomalous resistance terms [47]. Despite the need of this additional phase for Type-2 machines it is found that the dynamics up to the slow compression (pinch) phase and neutron and soft X-ray yields for the same Type-2 machines are correctly described by the 5-phase code which already incorporates a compensatory feature for the neutron yield, basically a multiplier to the beam deuteron energy deduced from inductive voltage and fitted with global experimental data (see section on neutron calculation below). The conclusion is that the anomalous resistance phase which dominates an additional phase after the pinch phase is needed to fit the current trace but otherwise is not needed for the description of the dynamics up to the pinch phase or for the estimation of the neutron and SXR yields.

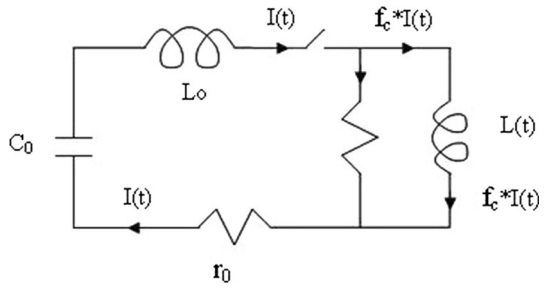

Fig. 3 Plasma focus circuit: the inductance of the plasma focus tube is treated as a time-dependent inductance L(t), neglecting the plasma resistance r_p. The resistance parallel to the L(t) mesh is a schematic representation of a leakage current $(1 - f_c)I(t)$ which limits the effective drive current to $f_c I(t)$

We proceed to a detailed description of the basic 5-phase model code.

The Equations of the 5-Phase Model

Axial Phase (Snow-Plow Model)

We refer to Fig. 2a, the left image of Fig. 2:

Rate of change of momentum at current sheath, position z, is

$$\frac{d}{dt}\left(\left[\rho_o\pi(b^2-a^2)z\right]f_m\frac{dz}{dt}\right)=\rho_o\pi(c^2-1)\,a^2f_m\frac{d}{dt}\left(z\frac{dz}{dt}\right)$$

Magnetic force on current sheath is

$$\int_a^b\left[\left(\frac{\mu I f_c}{2\pi r}\right)^2\Big/(2\mu)\right]2\pi r dr=\frac{\mu f_c^2}{4\pi}\ln(c)I^2$$

where f_m = fraction of mass swept down the tube in the axial direction; f_c = fraction of current flowing in piston (or current sheet CS); c = b/a = cathode radius/anode radius, ρ_0 = ambient density, I = time varying circuit current, μ = permeability.

Equation of Motion

From the above equating rate of change of momentum to the magnetic force, we derive:

$$\frac{d^2z}{dt^2}=\left[\frac{f_c^2}{f_m}\frac{\mu(\ln c)}{4\pi^2\rho_o(c^2-1)}\left(\frac{I}{a}\right)^2-\left(\frac{dz}{dt}\right)^2\right]\Big/z \qquad (1)$$

Circuit (Current) Equation

We ignore r(t), plasma resistance, hence not shown in the circuit diagram Fig. 3. This is the approximation which is generally used for electromagnetic drive. Using the C_0–L_0–L(t)–r_0 mesh of Fig. 3 we derive the circuit equation as follows:

$$\frac{d}{dt}[(L_o + Lf_c)I] + r_o I = V_o - \int \frac{Idt}{C_o}$$

$$\frac{dI}{dt} = \left[V_o - \frac{\int Idt}{C_o} - r_o I - If_c \frac{\mu}{2\pi}(\ln c)\frac{dz}{dt}\right] \Big/ \left[L_o + \frac{f_c \mu}{2\pi}(\ln c)z\right] \tag{2}$$

Equations (1) and (2) are the generating equations of the model. They contain the physics built into the model. They are coupled equations. The equation of motion is affected by the electric current I. The circuit equation is affected by the current sheath motion dz/dt and position z.

Normalising the Equations to Obtain Scaling Parameters

Replace variables t, z, I by non-dimensionalised quantities as follows:

$\tau = t/t_0$, $\zeta = z/z_0$ and $\iota = il/I_0$

where the normalising quantities z_0 = the length of the anode, $t_0 = (L_0/C_0)^{0.5}$ (note that $2\pi t_0$ is the periodic time of L_0–C_0 discharge circuit) and $I_0 = V_0/Z_0$ where $Z_0 = (L_0/C_0)^{0.5}$ is the surge impedance.

Normalising, we have:

Equation of Motion

$$\frac{d^2\zeta}{d\tau^2} = \left[\frac{f_c^2}{f_m}\frac{\mu \ln c}{4\pi^2 \rho_0 (c^2-1)}\left(\frac{I_0}{a}\right)^2 \frac{t_0^2}{z_0^2}\iota^2 - \left(\frac{d\zeta}{d\tau}\right)^2\right] \Big/ \zeta$$

which we write in the following form

$$\frac{d^2\zeta}{d\tau^2} = \frac{\left[\alpha^2 \iota^2 - \left(\frac{d\zeta}{d\tau}\right)^2\right]}{\zeta} \tag{3}$$

with

$$\alpha^2 = t_0^2/t_a^2 \tag{4}$$

$$t_a = \left[\frac{4\pi^2(c^2-1)}{\mu \ln c}\right]^{1/2} \frac{\sqrt{f_m}}{f_c}\frac{z_o}{(I_o/a)/\sqrt{\rho}} \tag{5}$$

which is identified as the characteristic axial transit time of the CS for the anode axial phase.

$$\alpha = (t_0/t_a) \tag{6}$$

is identified as the first scaling parameter being the ratio of characteristic electrical discharge time to the characteristic axial transit time. This scaling parameter is seen as an indicator of the matching of electrical drive time to the axial transit time for good energy transfer.

We further identify a characteristic axial transit speed $v_a = z_0/t_a$ where

$$v_a = \left[\frac{\mu \ln c}{4\pi^2(c^2-1)}\right]^{1/2} \frac{f_c}{\sqrt{f_m}}\frac{(I_0/a)}{\sqrt{\rho}} \tag{7}$$

The quantity $(I_0/a)/\rho^{0.5}$ is the S (speed or drive) factor [61] of the PF axial phase and as we shall see also the radial phase; and indeed for all electromagnetically driven devices.

Normalising the circuit (current) Equation, we have:

$$\frac{d\iota}{d\tau} = \left(1 - \int \iota d\tau - \beta\iota \frac{d\zeta}{d\tau} - \delta\iota\right) \Big/ (1 + \beta\zeta) \tag{8}$$

where

$$\beta = L_0/L_a \tag{9}$$

and $L_a = (\mu/2\pi)(\ln c)z_0$ is the inductance of the axial phase when CS reaches anode end $z = z_0$.

Thus this second scaling parameter has a great effect on the electrodynamics of the system.

The third scaling parameter $\delta = r_0/Z_0$ is the ratio of circuit stray resistance to surge impedance. This has a damping effect on the current.

Equations (3) and (8) are the generating equations (in normalized form) that are integrated step-by-step for the time variation of current ι and axial position ζ.

Calculate Voltage Across Input Terminals of Focus Tube

$$V = \frac{d}{dt}(LIf_c) = f_c I\frac{dL}{dt} + f_c L\frac{dI}{dt} \quad \text{where} \quad L = \frac{\mu}{2\pi}(l_n c)z \tag{10}$$

Normalised to capacitor voltage V_0 : $\upsilon = \dfrac{V}{V_o}$

$$= \beta\iota\frac{d\zeta}{d\tau} + \beta\zeta\frac{d_c}{d\tau} \tag{11}$$

Integration Scheme for Normalised Generating Equations (3) and (8)

Define initial conditions:

$\tau = 0,\ d\zeta/d\tau = 0,\ \zeta = 0,\ \tau = 0,\ \int \iota d\tau,\ d\iota/d\tau = 1,\ d^2\zeta/d\tau^2 = (2/3)^{0.5}\alpha$

Set time increment: $D = 0.001$; Increment time: $\tau = \tau + D$

Next step values are computed using the following linear approximations:

$$\begin{aligned} \frac{d\zeta}{d\tau} &= \frac{d\zeta}{d\tau} + \frac{d^2\zeta}{d\tau^2}D \\ \zeta &= \zeta + \frac{d\zeta}{d\tau}D \\ \iota &= \iota + \frac{d\iota}{d\tau}D \\ \int \iota d\tau &= \int \iota d\tau + \iota D \end{aligned} \tag{12}$$

Use new values of $d\zeta/d\tau$ ζ, ι and $\int \iota d\tau$ to calculate new generating values of $d\iota/d\tau$ and $d^2\zeta/d\tau$ using generating Eqs. (3) and (8). Increment time again and repeat calculations of next step values and new generating values. Continue procedure until $\zeta = 1$. Then go on to radial phase inward shock.

Radial Inward Shock Phase (Slug Model)

The snowplow model is used for axial phase just to obtain axial trajectory and speed (from which temperature may be deduced) and to obtain reasonable current profile. As the plasma structure is assumed to be infinitesimally thin, no information of density is contained in the physics of the equation of motion, although an estimate of density may be obtained by invoking additional mechanisms e.g. using shock wave theory [11, 12].

In the radial phase however, a snowplow model (with infinitesimally thin structure) would lead to all current flowing at $r = 0$, with infinite inductance and density. This is obviously unrealistic.

We thus replace the snow plow model by a slug model [12, 15]. In this model, the magnetic pressure drives a shock wave ahead of it, creating a space for the magnetic piston (also called current sheet CS) to move into. The speed of the inward radial shock front (see the left image of Fig. 2) is determined by the magnetic pressure (which depends on the drive current value and CS position r_p). A radius-time representation of the slug model is shown in Fig. 4.

The speed of the magnetic piston (CS) is determined by the first law of thermodynamics applied to the effective increase

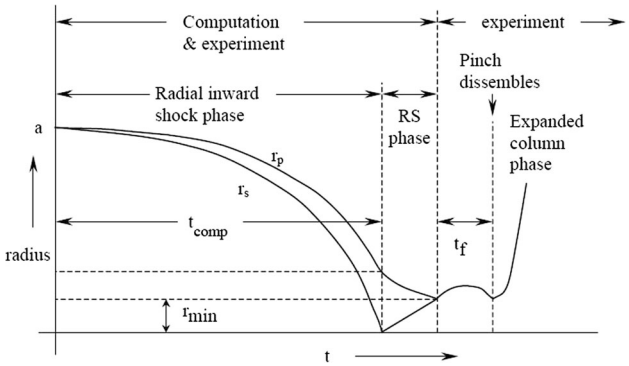

Fig. 4 Schematic of the radial phase- in radius versus time format

in volume between shock front SF and CS, created by the incremental motion of the SF. The compression is treated as an elongating pinch.

Four generating equations are needed to describe the motion of (a) radial SF (see Fig. 2b); (b) radial CS (c) pinch elongation and (d) the electric current; in order to be integrated for the four variables r_s, r_p, z_f and I.

Motion of Shock Front

From shock wave theory [11, 12].

$$\text{Shock pressure } P = 2\rho_0 v_s^2/(\gamma + 1) \tag{13}$$

where shock speed v_s into ambient gas ρ_0 causes the pressure of the shocked gas (just behind the shock front) to rise to value P (see Fig. 5); γ is the specific heat ratio of the gas.

If we assume that this pressure is uniform from the SF to the CS (infinite acoustic, or small disturbance speed approximation) then across the piston (Fig. 5), we may apply $P = P_m$ where

$$\begin{aligned} P_m &= \left(\mu I f_c/2\pi r_p\right)^2/2\mu \\ v_s^2 &= \frac{\mu(I f_c)^2}{8\pi^2 r_p^2} \times \frac{\gamma + 1}{2\rho_o f_{mr}} \end{aligned} \tag{13a}$$

where I is the circuit current and If_c is the current flowing in the cylindrical CS, taken as the same f_c as in the axial phase, and $\rho_0 f_{mr}$ is the effective mass density swept into the radial slug; where f_{mr} is a different (generally larger) factor than f_m of the axial phase.

$$\text{Thus } \frac{dr_s}{dt} = -\left[\frac{\mu(\gamma + 1)}{\rho_o}\right]^{1/2} \frac{f_c}{\sqrt{f_{mr}}} \frac{I}{4\pi r_p} \tag{14}$$

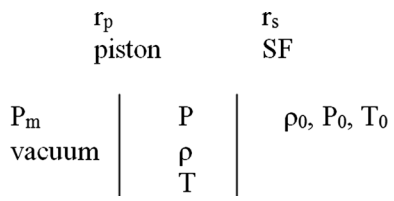

Fig. 5 Relationship between ambient conditions (quantities with *subscript* 0), slug and driver properties

Elongation Speed of CS (Open-Ended at Both Ends)

The radial compression is open-ended. Hence an axial shock is propagated in the z-direction, towards the downstream anode axis. We take z_f as the position of the axial CS. The pressure driving the axial shock is the same as the pressure driving the inward radial shock. Thus the axial shock speed is the same as the radial shock speed. The CS speed is slower, from shock wave theory, by an approximate factor of 2/(γ+1). Thus the axial elongation speed of the CS is:

$$\frac{dz_f}{dt} = -\left(\frac{2}{\gamma+1}\right)\frac{dr_s}{dt} \tag{15}$$

Radial Piston Motion

We inquire: for an incremental motion, dr_s, of the shock front, at a driving current I, what is the relationship between plasma slug pressure P and plasma slug volume Vol?

We assume an adiabatic relationship [12, 15] (assuming infinite small disturbance speed—for which we will apply a correction subsequently) to a fixed mass of gas in the slug during the incremental motion dr_s. We have $PVol^{\gamma} = $ constant or

$$\frac{\gamma dVol}{v} + \frac{dP}{P} = 0 \tag{16}$$

where slug pressure $P \sim v_s^2$ (see Eq. 13); so $\frac{dP}{P} = \frac{2dv_s}{v_s}$ but $v_s \sim \frac{I}{r_p}$ (see Eq. 13a);

so

$$\frac{dP}{P} = 2\left(\frac{dI}{I} - \frac{dr_p}{r_p}\right) \tag{16a}$$

Now slug volume $Vol = \pi (r_p^2 - r_s^2)\, z_f$.

Here we note that although the motion of the piston dr_p does not change the mass of gas in the slug, the motion of the shock front, dr_s, does sweep in an amount of ambient gas. This amount swept in is equal to the ambient gas swept through by the shock front in its motion dr_s. This swept-up gas is compressed by a ratio $(\gamma + 1)/(\gamma - 1)$ and will occupy part of the increase in volume dVol.

The actual increase in volume available to the original mass of gas in volume Vol does not correspond to increment dr_s but to an effective (reduced) increment drs (2/(γ+1)). (Note γ is specific heat ratio of the plasma e.g. γ = 5/3 for atomic gas, γ = 7/5 for molecular gas; for strongly ionising argon γ has value closer to 1 e.g. 1.15.) The specific heat ratio and effective charge Z_{eff} where needed are computed from a corona model and placed in the code in the form of a series of polynomials. This is described in the "Slow Compression (Pinch) Phase" section. Thus:

$$dVol = 2\pi\left(r_p dr_p - \frac{2}{\gamma+1} r_s dr_s\right) z_f + \pi\left(r_p^2 - r_s^2\right) dz_f$$

and we have:

$$\frac{\gamma dVol}{Vol} = \frac{2\gamma\left(r_p dr_p - \frac{2}{\gamma+1} r_s dr_s\right) z_f + \gamma\left(r_p^2 - r_s^2\right) dz_f}{z_f\left(r_p^2 - r_s^2\right)} \tag{16b}$$

From Eqs. (16, 16a and 16b); we have

$$\frac{dr_p}{dt} = \frac{\frac{2}{\gamma+1}\frac{r_s}{r_p}\frac{dr_s}{dt} - \frac{r_p}{\gamma I}\left(1 - \frac{r_s^2}{r_p^2}\right)\frac{dI}{dt} - \frac{r_p}{z_f}\left(1 - \frac{r_s^2}{r_p^2}\right)\frac{dz_f}{dt}}{\frac{\gamma-1}{\gamma} + \frac{1}{\gamma}\frac{r_s^2}{r_p^2}} \tag{17}$$

Circuit Equation During Radial Phase

The inductance of the focus tube now consists of the full inductance of the axial phase and the inductance of the radially imploding and elongating plasma pinch.

Thus

$$L = \frac{\mu}{2\pi}(\ln c) z_o + \frac{\mu}{2\pi}\left(\ln\frac{b}{r_p}\right) z_f \tag{18}$$

where both z_f and r_p vary with time.

Thus the circuit (current) equation is obtained as:

$$\frac{dI}{dt} = \frac{V_o - \frac{\int I dt}{C_o} - r_o I - f_c \frac{\mu}{2\pi}\left(\ln\frac{b}{r_p}\right) I \frac{dz_f}{dt} + f_c \frac{\mu}{2\pi}\frac{z_f}{r_p} I \frac{dr_p}{dt}}{L_o + f_c \frac{\mu}{2\pi}(\ln c) z_o + f_c \frac{\mu}{2\pi}\left(\ln\frac{b}{r_p}\right) z_f} \tag{19}$$

The four generating Eqs. (14, 15, 17, 19) form a closed set of equations which may be integrated for r_s, r_p, z_f and I.

Normalization

For this phase the following normalization is adopted.

$\tau = t/t_o$, $\iota = I/I_o$ as in axial phase but with $\kappa_s = r_s/a$, $\kappa_p = r_p/a$, $\zeta_f = z_f/a$ ie. Distances are normalized to anode radius, instead of anode length. After normalization we have:

$$\text{Radial shock speed} \quad \frac{d\kappa_s}{d\tau} = -\alpha\alpha_1 \iota/\kappa_p \tag{20}$$

Axial column elongation speed (both ends of column defined by axial piston)

$$\frac{d\zeta_f}{d\tau} = -\frac{2}{\gamma+1}\frac{d\kappa_s}{d\tau} \tag{21}$$

Radial piston speed :

$$\frac{d\kappa_p}{d\tau} = \frac{\frac{2}{\gamma+1}\frac{\kappa_s}{\kappa_p}\frac{d\kappa_s}{d\tau} - \frac{\kappa_p}{\gamma\iota}\left(1-\frac{\kappa_s^2}{\kappa_p^2}\right)\frac{d\iota}{d\tau} - \frac{1}{\gamma+1}\frac{\kappa_p}{\zeta_f}\left(1-\frac{\kappa_s^2}{\kappa_p^2}\right)\frac{d\zeta_f}{d\tau}}{(\gamma-1)/\gamma + (1/\gamma)(\kappa_s^2/\kappa_p^2)} \tag{22}$$

Current :

$$\frac{d\iota}{d\tau} = \frac{1 - \int \iota d\tau + \beta_1\left[\ln(\kappa_p/c)\right]\iota\frac{d\zeta_f}{d\tau} + \beta_1\frac{\zeta_f\iota}{k_p}\frac{d\kappa_p}{d\tau} - \delta\iota}{\left\{1+\beta-(\beta_1)\left[\ln\left(\kappa_p/c\right)\right]\zeta_f\right\}} \tag{23}$$

where scaling parameters are

$$\beta_1 = \beta/(\text{Flnc}) \tag{24}$$

and

$$\alpha_1 = \left[(\gamma+1)(c^2-1)/(4\ln c)\right]^{1/2} F[f_m/f_{mr}]^{1/2}. \tag{24a}$$

We note that $F = z_0/a$ (the length/radius ratio of the anode) may be considered to be the controlling parameter of β_1 and α_1. In other words, β_1 and α_1 may not be independently assigned, but should be assigned as a pair with the value of each fixed by the value of F.

Note that whereas we interpret $\alpha = t_0/t_a$, Eq. (6) we may interpret

$$\alpha_1 = t_a/t_r \tag{25}$$

where t_r is the characteristic radial transit time.

$$t_r = \frac{4\pi}{[\mu(\gamma+1)]^{1/2}}\frac{\sqrt{f_{mr}}}{f_c}\frac{a}{(I_0/a)/\sqrt{\rho}} \tag{26}$$

The product $\alpha\alpha_1$ may then be interpreted as $\alpha\alpha_1 = \frac{t_o}{t_a} = t_o/t_r$

The characteristic speed of the radial inward shock to reach focus axis is:

$$v_r = a/t_r = \frac{[\mu(\gamma+1)]^{1/2}}{4\pi}\frac{f_c}{\sqrt{f_{mr}}}\frac{(I_o/a)}{\sqrt{\rho}} \tag{27}$$

The ratio of characteristic radial and axial speeds is also essentially a geometrical one, modified by thermodynamics. It is

$$v_r/v_a = \left[\frac{(c^2-1)(\gamma+1)}{4\ln c}\right]^{1/2} \tag{28}$$

with a value typically 2.5 for a small deuterium PF with c $\sim$3.4, $\gamma = 5/3$. We note [61] that the radial characteristic speed has same dependence as axial transit speed on drive factor (see Eq. 7) $S = (I_o/a)/\sqrt{\rho}$.

Calculate Voltage V Across PF Input Terminals

As in the axial phase, the tube voltage is taken to be inductive: V = d(LI)/dt where $L = \frac{\mu}{2\pi}(\ln c)z_0 + \frac{\mu}{2\pi}\left(\ln\frac{b}{r_p}\right)z_f$

$$V = \frac{\mu}{2\pi}\left[(\ln c)z_o + \left(\ln\frac{b}{r_p}\right)z_f\right]f_c\frac{dI}{dt} + \frac{\mu}{2\pi}\left[\left(\ln\frac{b}{r_p}\right)\frac{dz_f}{dt} - \frac{z_f}{r_p}\frac{dr_p}{dt}\right]f_c I \tag{29}$$

We may also normalize to the charge voltage V_0; so that $\upsilon = V/V_o$

$$v = \left[\beta - \beta_1\left(\ln\frac{\kappa_p}{c}\right)\zeta_f\right]\frac{d\iota}{d\tau} - \beta_1\iota\left[\left(\frac{\zeta_f}{\kappa_p}\right)\frac{d\kappa_p}{d\tau} + \left(\ln\frac{\kappa_p}{c}\right)\frac{d\zeta_f}{d\tau}\right] \tag{30}$$

Integrating for the Radial Inward Shock Phase

The 4 normalised generating Eqs. (20–23) may now be integrated using the following initial conditions: $\tau =$ the time that axial phase ended, $\kappa_s = 1$, $\kappa_p = 1$, $\zeta_f = 0$ (taken as a small number such as 0.00001 to avoid numerical difficulties for Eq. (21)). $\iota =$ value of current at end of the axial phase; $\int\iota d\tau =$ value of 'flowed charge' at end of axial phase. Smaller time increments of D = 0.001/100) are taken.

$\frac{d\kappa_s}{d\tau}$, $\frac{d\zeta_f}{d\tau}$, $\frac{d\kappa_p}{d\tau}$ and $\frac{d\iota}{d\tau}$ are sequentially calculated from generating Eqs. (20–23)

Then using linear approximations we obtain:

$\kappa_s = \kappa_s + \text{Dd}\kappa_s/\text{d}\tau$; $\zeta_f = \zeta_f + \text{Dd}\zeta_f/\text{d}\tau$; $\kappa_p = \kappa_p + \text{Dd}\kappa_p/\text{d}\tau$; $\iota = \iota + \text{Dd}\iota/\text{d}\tau$ and $\int\iota d\tau = \int\iota d\tau + \iota D$

Time is then incremented by D, and the next step value of dks/dt, dzf/dt, dkp/dt and di/dt are computed from (30–23) followed by linear approximation for κ_s, ζ_f, κ_ρ, ι and $\int \iota d\tau$.

The sequence is repeated step-by-step until $\kappa_s = 0$.

Correction for Finite Acoustic (Small Disturbance) Speed

In the slug model above we assume that the pressure exerted by the magnetic piston (current I, position r_p) is instantaneously felt by the shock front (position r_s). Likewise the shock speed dr_s/d_t is instantaneously felt by the piston (CS). This assumption of infinite small disturbance speed (SDS) is implicit in Eqs. (14 and 17) (or in normalised form Eqs. (20 and 22).

Since the SDS is finite, there is actually a time lapse Δt communicating between the SF and CS. This communication delay has to be incorporated into the model. Otherwise for the PF, the computation will yield too high values of CS and SF speed.

Consider the instant t, SF is at r_s, CS at r_p, value of current is I. SF actually feels the effect of the current not of value I but of a value I_{delay} which flowed at time $(t - \Delta t)$, with the CS at r_{pdelay}. Similarly the piston 'feels' the SF speed is not dr_s/d_t but $(dr_s/d_t)_{delay}$ at time $(t - \Delta t)$.

To implement this finite SDS correction we adopt the following procedure:

Calculate the SDS, taken as the acoustic speed.

$$SDS = \left(\frac{\gamma P}{\rho}\right)^{1/2} \text{ or } \left(\frac{\gamma R_0}{M} D_c T\right)^{1/2} \text{ or } \left(\frac{\gamma D_c kT}{M m_i}\right)^{1/2} \quad (31)$$

where M = molecule weight, R_0 = Universal gas constant = 8×10^3 (SI units), m_i = mass of proton, k = Boltzmanns constant. D_c = departure coefficient = DN (1 + Z).

Where Z, here, is the effective charge of the plasma $Z = \sum {}^{J}_{r} r\alpha_r$, summed over all ionization levels r = 1… J. This is computed using a corona model. The procedure is described in more details in the description of the pinch phase.

DN = dissociation number, e.g. for Deuterium DN = 2, whereas for argon DN = 1.

From shock theory, the temperature T may be computed for the shocked plasma as

$$T = \frac{M}{RoD} \frac{2(\gamma - 1)}{(\gamma + 1)^2} \left(\frac{dr_s}{dt}\right)^2 \quad (32)$$

The communication delay time is then:

$$\Delta T = (r_p - r_s)/SDS \quad (33)$$

In our programme using the Microsoft EXCEL VISUAL BASIC, data of the step-by-step integration is stored row-by-row, each step corresponding to one row. Thus the ΔT may be converted to Δ (row number) by using Δ (row number) = ΔT/(timestep increment); this Δ (row number) being, of course, rounded off to an integer.

The correction then involves 'looking back' to the relevant row number to extract the corrected values of I_{delay}, r_{pdelay}, $(dr_s/dt)_{delay}$. Thus in the actual numerical integration, in Eq. (20) ι and κ_p are replaced by ι_{delay} and κ_{pdelay} and in Eq. (22) dk_s/dt is replaced by $(dk_s/dt)_{delay}$.

Radial Reflected Shock (RS) Phase

When the inward radial shock hits the axis, $\kappa_s = 0$. Thus in the computation, when $\kappa_s \leq 1$ we exit from radial inward shock phase. We start computing the RS phase.

The RS is given a constant speed of 0.3 of on-axis inward radial shock speed [11, 12].

In this phase computation is carried out in real (SI) units.

Reflected Shock Speed

$$\frac{dr_r}{dt} = -0.3\left(\frac{dr_s}{dt}\right)_{on-axis} \quad (34)$$

Piston Speed

$$\frac{dr_p}{dt} = \frac{-\frac{r_p}{\gamma I}\left(1 - \frac{r_s^2}{r_p^2}\right)\frac{dI}{dt} - \frac{r_p}{z_f}\left(1 - \frac{r_s^2}{r_p^2}\right)\frac{dz_f}{dt}}{\frac{\gamma - 1}{\gamma} + \frac{1}{\gamma}\frac{r_s^2}{r_p^2}} \quad (35)$$

Elongation Speed

$$\frac{dz_f}{dt} = -\left(\frac{2}{\gamma + 1}\right)\left(\frac{dr_s}{dt}\right)_{on-axis} \quad (36)$$

Circuit Equation

$$\frac{\frac{dI}{dt} = V_o - \frac{\int I dt}{C_o} - r_o I - f_c \frac{\mu}{2\pi}\left(\ln \frac{b}{r_p}\right) I \frac{dz_f}{dt} + f_c \frac{\mu}{2\pi}\frac{z_f}{r_p} I \frac{dr_p}{dt}}{L_o + f_c \frac{\mu}{2\pi}(\ln c) z_o + f_c \frac{\mu}{2\pi}\left(\ln \frac{b}{r_p}\right) z_f} \quad (37)$$

The integration of these four coupled generating Eqs. (34–37) is carried out step-by-step as in the radial inward shock phase.

Tube Voltage

The tube voltage uses Eq. (29) above as in the radial inward shock phase.

In this phase as the RS (position r_r) moves outwards, the piston (position r_p) continues moving inwards. When the RS position reaches that of the piston the RS phase ends and the slow compression (pinch) phase begins.

Slow Compression (Pinch) Phase

In this phase the piston speed is:

$$\frac{dr_p}{dt} = \frac{\frac{-r_p}{\gamma I}\frac{dI}{dt} - \frac{1}{\gamma+1}\frac{r_p}{z_f}\frac{dz_f}{\mathrm{dt}} + \frac{4\pi(\gamma-1)}{\mu\gamma z_f}\frac{r_p}{\mathrm{f_c^2}I^2}\frac{dQ}{dt}}{\frac{\gamma-1}{\gamma}} \tag{38}$$

Here we have included energy loss/gain terms into the equation of motion. The plasma gains energy from Joule heating; and loses energy through Bremsstrahlung and line radiation. A positive power term dQ/dt will tend to push the piston outwards whilst a power loss term will have the opposite effect. The specific heat ratio γ is taken as 5/3 for H, D, T and He gases. For other gases such as Ne, N, O, Ar, Kr, Xe, a sub-routine [62] based on a corona model is used to compute γ as a function of temperature; and for faster computing the values of γ for each gas are represented by a series of polynomials incorporated into the code. At the same time the charge number Z is also computed and included as another series of polynomials and incorporated into the code.

The Joule term is calculated from the following:

$$\frac{dQ_J}{dt} = RI^2 f_c^2 \tag{39}$$

where plasma resistance R is calculated using the Spitzer form [63]:

$$R = \frac{1,290 Z z_f}{\pi r_p^2 T^{3/2}} \tag{40}$$

And using Bennett [64] form: temperature

$$T = \frac{\mu}{8\pi^2 k} I^2 f_c^2 / (D N_o a^2 f_{mr}) \tag{41}$$

The Bremsstrahlung loss term may be written as:

$$\frac{dQ_B}{dt} = -1.6 \times 10^{-40} N_i^2 \left(\pi r_p^2\right) z_f T^{1/2} Z^3 \tag{42}$$

$$N_o = 6 \times 10^{26} \frac{\rho_o}{M}; \quad N_i = N_a f_{mr} \left(\frac{a}{r_p}\right)^2 \tag{43}$$

In the above, Z_n = atomic number, N_0 = ambient number density, N_i = ion number density.

The line loss term may be written as:

$$\frac{dQ_L}{dt} = -4.6 \times 10^{-31} N_i^2 Z Z_n^4 \left(\pi r_p^2\right) z_f / T \tag{44}$$

$$\text{And} \quad \mathrm{dQ/dt} = \mathrm{dQ_J/dt} + \mathrm{dQ_B/dt} + \mathrm{dQ_L/dt} \tag{45}$$

where dQ/dt is the total power gain/loss of the plasma column

By this coupling, if, for example, the radiation loss $dQ_B/dt + dQ_L/dt$ is severe, this would lead to a large value of dr_p/dt inwards. In the extreme case, this leads to radiation collapse [40], with r_p going rapidly to such small values that the plasma becomes opaque to the outgoing radiation, thus stopping the radiation loss.

This radiation collapse occurs at a critical current of 1.6 MA (the Pease–Braginski current) for deuterium [65, 66]. For gases such as Neon or Argon, because of intense line radiation, the critical current is reduced to even below 100 kA, depending on the plasma temperature [40, 67].

Plasma Self Absorption and Transition from Volumetric Emission to Surface Emission

Plasma self-absorption [12, 68, 69] and volumetric (emission described above) to surface emission of the pinch column are implemented in the following manner.

The photonic excitation number is written as follows:

$$\mathrm{M} = 1.66 \times 10^{-15} \mathrm{r_p Z_n^{0.5} n_i / \left(Z\ T^{1.5}\right)} \tag{46}$$

with T in eV, rest in SI units

The volumetric plasma self-absorption correction factor A is obtained as follows::

$$\mathrm{A_1 = \left((1 + 10^{-14} n_i Z) / (T^{3.5})\right); \quad A_2 = 1 / A_1; \quad A = A_2^{(1+M)}} \tag{47}$$

Transition from volumetric to surface emission occurs when the absorption correction factor goes from 1 (no absorption) down to 1/e (e = 2.718) when the emission becomes surface-like given by::

$$\frac{dQ_L}{dt} = -const Z^{0.5} Z_n^{3.5} r_p z_f T^4 \tag{48}$$

where the constant 'const' is taken as 4.62×10^{-16} to conform with numerical experimental observations that this value enables the smoothest transition, in general, in terms of power values from volumetric to surface emission.

Neutron Yield

Neutron yield is calculated with two components, thermonuclear term and beam-target term.

The thermonuclear term is taken as:

$$dYth = 0.5 n_i^2 \pi r_p^2 z_f < \sigma v > (\text{time interval}) \quad (49)$$

where $<\sigma v>$ is the thermalized fusion cross section-velocity product corresponding to the plasma temperature [70], for the time interval under consideration. The yield Yth is obtained by summing up over all intervals during the focus pinch.

The beam-target term is derived using the following phenomenological beam-target neutron generating mechanism [71], incorporated in the code version RADPFV5.13 and later. A beam of fast deuteron ions is produced by diode action in a thin layer close to the anode, with plasma disruptions generating the necessary high voltages. The beam interacts with the hot dense plasma of the focus pinch column to produce the fusion neutrons. In this modeling each factor contributing to the yield is estimated as a proportional quantity and the yield is obtained as an expression with proportionality constant. The yield is then calibrated against a known experimental point.

The beam-target yield is written in the form: $Y_{b-t} \sim n_b\, n_i\, (r_p^2 z_p)\, (\sigma\, v_b)\, \tau$

Where n_b is the number of beam ions per unit plasma volume, n_i is the ion density, r_p is the radius of the plasma pinch with length z_p, σ the cross-section of the D–D fusion reaction, n-branch [71], v_b the beam ion speed and τ is the beam-target interaction time assumed proportional to the confinement time of the plasma column. Total beam energy is estimated [71] as proportional to $L_p I_{pinch}^2$, a measure of the pinch inductance energy, L_p being the focus pinch inductance. Thus the number of beam ions is $N_b \sim L_p I_{pinch}^2/v_b^2$ and n_b is N_b divided by the focus pinch volume. Note that $L_p \sim \ln(b/r_p) z_p$, that [61] $\tau \sim r_p \sim z_p$, and that $v_b \sim U^{1/2}$ where U is the disruption-caused diode voltage. Here 'b' is the cathode radius. We also assume reasonably that U is proportional to V_{max}, the maximum voltage induced by the current sheet collapsing radially towards the axis.

Hence we derive

$$Y_{b-t} = C_n n_i I_{pinch}^2 z_p^2 \left((\ln b/r_p)\right) \sigma / V_{max}^{1/2} \quad (50)$$

where I_{pinch} is the current flowing through the pinch at start of the slow compression phase; r_p and z_p are the pinch dimensions at end of that phase. Here C_n is a constant which in practice we will calibrate with an experimental point.

The D–D cross-section is highly sensitive to the beam energy so it is necessary to use the appropriate range of beam energy to compute σ. The code computes V_{max} of the order of 20–50 kV. However it is known [71], from experiments that the ion energy responsible for the beam-target neutrons is in the range 50–150 keV, and for smaller lower-voltage machines the relevant energy [72, 73] could be lower at 30–60 keV. Thus to align with experimental observations the D–D cross section σ is reasonably obtained by using beam energy fitted to 3 times V_{max}.

A plot of experimentally measured neutron yield Y_n versus I_{pinch} was made combining all available experimental data [7, 8, 22, 61, 71–76]. This gave a fit of $Y_n = 9 \times 10^{10} I_{pinch}^{3.8}$ for I_{pinch} in the range 0.1–1 MA [38, 52–54]. From this plot a calibration point was chosen at 0.5 MA, $Y_n = 7 \times 10^9$ neutrons. The model code [12] from version RADPFV5.13 onwards was thus calibrated to compute Y_{b-t} which in our model is the same as Y_n.

Column Elongation

Whereas in the radial RS phase we have adopted a 'frozen' elongation speed model, we now allow the elongation to be driven fully by the plasma pressure.

$$\frac{dz_f}{dt} = \left[\frac{\mu}{4\pi^2(\gamma+1)\rho_o}\right]^{1/2} \frac{I f_c}{r_p} \quad (51)$$

Circuit Current Equation

$$\frac{dI}{dt} = \frac{V_o - \frac{\int I dt}{C_o} - \frac{\mu}{2\pi}\left(\ln\frac{b}{r_p}\right)\frac{dz_f}{dt} I f_c + \frac{\mu}{2\pi}\frac{z_f}{r_p}\frac{dr_p}{dt} I f_c - I(R f_c + r_o)}{L_o + \frac{\mu}{2\pi} f_c \left((\ln c) z_o + \left(\ln\frac{b}{r_p}\right) z_f\right)} \quad (52)$$

Voltage Across Focus Terminals

$$V = \frac{\mu f_c}{2\pi} I \left[\left(\ln\frac{b}{r_p}\right)\frac{dz_f}{dt} - \frac{z_f}{r_p}\frac{dr_p}{dt}\right] + \frac{\mu f_c}{2\pi}\left[\left(\ln\frac{b}{r_p}\right) z_f + (\ln C) z_o\right]\frac{dI}{dt} + RI \quad (53)$$

Pinch Phase Dynamics and Yields of Neutrons, Soft X-rays, Ion Beams and Fast Plasma Stream

Equations (38), (51) and (52) are integrated as coupled equations for r_p, z_f and I. At each step the value of dQ/dt is also evaluated as above using Eqs. (39)–(45) with the effect of plasma self-absorption implemented using Eqs. (46)–(48). Soft X-rays of various gases are computed using Eq. (44) modified by the effect of plasma self-absorption.

Neutron yield is computed using Eq. (50) and Eq. (49). In the latest version RADPFV5.15FIB [12] fast ion beam (FIB) fluence and flux, energy fluence and flux, power flow and damage factors as well as fast plasma streams (FPS) exiting the pinch are also computed [50, 51].

The step-by-step integration is terminated at the end of a period related to the transit time of small disturbance speed across the plasma pinch column.

Expanded Column Axial Phase

We model the expanded column axial phase [12, 26] in the following manner.

In the expanded column phase we assume that the current flows uniformly from anode to cathode in a uniform column having the same radius as the anode and a length of z.

The normalised equations (same normalisation as in axial phase):

$$\text{Circuit current}: \quad \frac{d\imath}{d\tau} = \frac{1 - \int \imath d\tau - \beta\imath \frac{d\zeta}{d\tau} e - \delta\imath}{1 + \beta + \beta(\zeta - 1)e} \tag{54}$$

$$\text{where } e = \left(\ln c + \tfrac{1}{z}\right) \Big/ \ln c$$

$$\text{Motion}: \quad \frac{d^2\zeta}{d\tau^2} = \frac{\alpha^2 \imath^2 e_1 - h^2 \left(\frac{d\zeta}{d\tau}\right)^2}{1 + h^2(\zeta - 1)} \tag{55}$$

$$h = \left[c^2/(c^2 - 1)\right]^{1/2}$$

$$e_1 = \left(\ln c + \frac{1}{4}\right) \Big/ (\ln c)$$

The initial conditions for ι and $\int \imath d\tau$ are the last values of ι and $\int \imath d\tau$ from the last phase. The initial value of ζ is $\zeta = 1 + \zeta_f$ where ζ_f is the last length of the focus column, but normalised to z_o, rather than 'a'. This phase is terminated when the discharge has proceeded to a half cycle. The purpose of computing this phase is to allow the fitting of the computed current to the measured to the point when the current has dropped to low levels beyond interest. This completes the integration of all five phases.

Procedure for Using the Code

The Lee model code is configured [12, 30, 52–54] to work as any PF by inputting: bank parameters, L_0, C_0 and stray circuit resistance r_0; tube parameters b, a and z_0 and operational parameters V_0 and P_0 and the fill gas.

The computed total current waveform is fitted to a measured waveform by varying model parameters f_m, f_c, f_{mr} and f_{cr} sequentially, until the computed waveform agrees with the measured waveform [12, 52]. The fitting procedure is described more fully in the following paragraph.

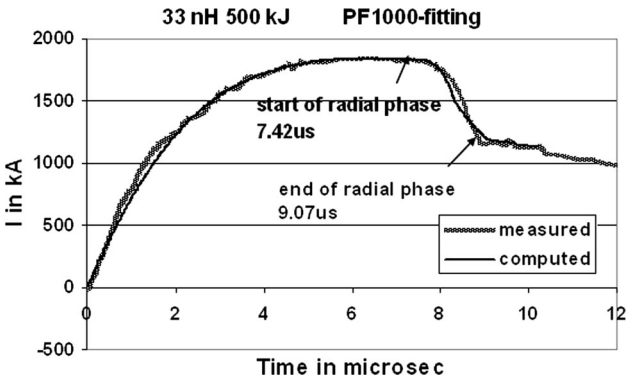

Fig. 6 A typical 5-phase fit of a low inductance PF; showing reasonable agreement between computed and measured waveforms

First, the axial model factors f_m, f_c are adjusted (fitted) until the features (a) computed rising slope of the total current trace and (b) the rounding off of the peak current as well as (c) the peak current itself are in reasonable (typically very good) fit with the measured total current trace. Then the radial phase model factors f_{mr} and f_{cr} are adjusted sequentially until (d) the computed slope of the current dip and (e) the depth of the dip agree with the measured. Note that the fitting of the computed trace with the measured current trace is done up to the end of the radial phase which is typically at the bottom of the current dip (for example, see Fig. 6. Fitting of the computed and measured current traces beyond this point is not done. If there is significant divergence of the computed with the measured trace beyond the end of the radial phase, this divergence is not considered important. Once fitted the code outputs in tabular and graphical forms [12, 52] realistic data of the following: axial and radial dynamics (positions and speeds), pinch length and minimum pinch radius, temperatures and densities, Bremsstrahlung and line yields, thermonuclear and beam-target neutron yields, fast ion beam flux and fluence, energy flux and fluence, power flow and damage factors, fast plasma stream energies and speeds [50, 51]. Also energy distributions and thermodynamics properties are found to be realistic representations of the actual machines.

This concludes the description of the standard 5-phase Lee model code. This 5-phase code has been used to fit all low L_0 PF with adequate accuracy (an example is given in Fig. 6 below). However it was found necessary for high L_0 PF devices to include a 6-phase (phase 4a) in order to achieve a complete fit. The development of the code variant version (RADPFV6.1b) [12] for phase 4a is described in the following section.

Adding a 6th Phase: From Pinch (Slow Compression) Phase to Large Volume Plasma Phase: The Transition Phase 4a

From experiments, it is well known that after a brief period (few ns for a small PF), the quiescent column is rapidly broken up by instabilities. One effect is a huge spike of voltage, partially observed at focus tube terminals. This voltage spike is responsible for driving ion beams (forward direction) and REB (negative direction, up the anode) with energies typically 200 keV. The final result of this instability mechanism is the breaking up of the focus pinch into a large expanded current column.

The 5-Phase Model is Adequate for Low Inductance L_0 Plasma Focus Devices

The 5-phase Lee code does not model the transition from Phase 4 to Phase 5. Nevertheless it has been found to be adequate for modelling all the well-known PF with low static inductance L_0 [18, 22, 29, 34–39, 47] which we have fitted; in the sense that the computed current traces can be fitted to the measured current trace by adjustment of the model parameters f_m, f_c, f_{mr} and f_{cr}. This has been the case for the PF1000, PF400J, NX1, NX2, DPF78, Poseidon [42], FMPF1 [77, 78], FN-II [35]. An example of a typical 5-phase fit is shown in Fig. 6.

The 5-Phase Model is Not Adequate for High L_0 Plasma Focus Devices

Amongst the well-published PF devices only the UNU/ICTP PFF [7–9] which has relatively higher L_0 of 110 nH presented problem in the fitting. This was due to a very small computed current dip and a measured current dip that has always been masked by very large oscillations taken to be noise; although when operated in unusually low pressure regime, a clear discrepancy was noted between the computed and measured current trace [79, 80].

In 2012 a current trace from the then newly commissioned KSU DPF (Kansas State University Dense Plasma Focus) [25] which had an even higher L_0, was obtained by numerically integrating the output of a *dI/dt* coil. An analysis of the frequency response of the coil system and the DSO signal acquisition system showed that noise frequencies below 200 MHz were removed by the numerical integration. The resultant waveform is clean and clearly shows an extended current dip with good depth and duration (see Fig. 7, the darker trace). The KSU DPF shows very consistent operation with more than 95 % of the shots showing current dips with similar depth and duration.

Following the usual procedure of the Lee model code, an attempt was made to fit the computed current trace with the measured. The computed current trace has only a small dip as is characteristic of the computed current dip of a device with large static inductance L_0. All possible adjustments were made to the model parameters but the computed current dip could not be made to fit the whole measured current dip. The best fit is shown in Fig. 7; which shows that the computed dip does fit the first small part of the measured current dip. But the measured dip continues on in both depth and duration far beyond the computed dip.

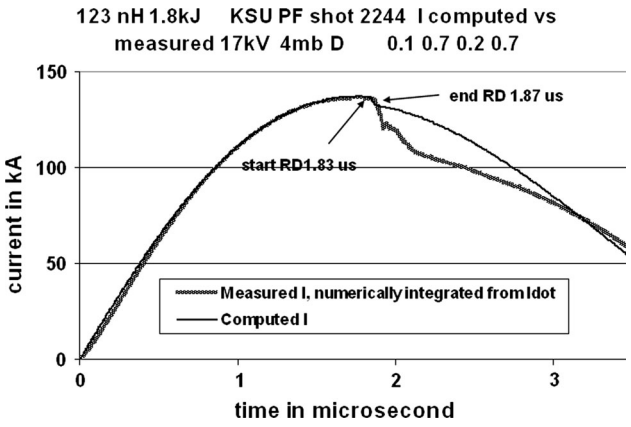

Fig. 7 Computed current trace (*lighter trace*) with best attempt to fit to the measured current trace (*darker trace*)

Factors Distinguishing the Two Types of Plasma Focus Devices

The code models the electrodynamic situation using the slug model and a reflected shock for the radial phase, ending the radial phase in phase 4. Let's call the radial phase modeled in that manner as the REGULAR radial phase. This REGULAR radial phase, in increasing sharply the inductance of the system (constituting also a dynamic resistance [38, 39]) causes a dip on the current trace. Call this the regular dip *RD*. At the end of the REGULAR radial phase experimental observations point to another phase [5], which we shall call phase 4a, (i.e. after phase 4, but before the final axial phase 5), of 'instabilities' manifesting in anomalous resistance. These effects would also extract energy from the magnetic field and hence produce further current dips. These effects are not modeled specifically in the code. Call this the extended current dip *ED*.

However it may be argued that as long as the model parameters can be stretched sufficiently to have the computed current dip agree with the measured current dip, then in a gross sense, the modelling is energetically and mass-wise equivalent to the physical situation. Then the resulting gross characteristics from the model would give a fair representation of the actual plasma properties, even though the model has not specifically modeled *ED*. In other words

RD is able to be stretched to also model *ED*, with equivalent energetics and mass implications. Whether *RD* can be stretched sufficiently to cover *ED* depends on the relative sizes of the two effects. If *RD* is already a big dip, then this effect may dominate and it is more likely that *RD* may be stretched sufficiently to cover the less prominent *ED*. If *RD* is only a miniscule dip and *ED* is a big dip, then it is unlikely that the *RD* can be stretched enough to encompass the *ED*.

We looked at the inductance L_0, and the ratio of L_0 with various inductances inherent in the system. We considered the inductance ratio $R_L = (L_0 + L_a)/L_{pinch}$ where L_{pinch} is the inductance of the focus pinch at the end of the REGULAR radial phase, L_0 the bank static inductance and L_a the inductance of the axial part of the focus tube. We also considered the remnant energy ratio $R_{EL} = (E_{L0} + E_{La})/E_{Lpinch}$ where E_{L0} = energy stored in L_0 at end of the *RD*, E_{La} = energy stored in L_a at end of the *RD* and E_{Lpinch} = energy stored inductively in the pinch at end of *RD*.

Computing the values of these two quantities for PF1000, Poseidon, DPF78, NX2, PF400 J, FMPF-1, FNII and UNU/ICTPPFF and KSU PF, we have a range of devices from very big (MJ) to rather small (sub kJ) of which we have well documented fittings.

The results show that the smaller is the ratio R_L, the bigger is the regular current dip (*RD*). When this ratio is large (primarily due to a large L_0 in the numerator), like in the case of KSU PF, the REGULAR radial phase RD is miniscule. Likewise, the trend is also observed for the ratio R_{EL}. The smaller this energy ratio, the bigger is the current dip.

On the basis of these two ratios we have divided the PF devices into two types: T1 and T2. Type T1 are for PF devices with relatively small L_0 with large RD's and with relatively small ratios R_L and R_{EL}. These T1 focus devices are well-fitted using the Lee model code. The computed current traces (with radial phase computed only as a regular dip RD) are well-fitted to the whole measured current trace. Type *T*2 are for PF devices with relatively large L_0 with small *RD*'s and with relatively large ratios of R_L and R_{EL}. These *T*2 focus devices are not well-fitted using the Lee model code. The computed current trace shows only a small dip which is fitted to the first portion of the measured current dip; but the measured current dip has an extended portion which is not well-fitted using the 5-phase Lee model code.

Next we note that the magnetic energy per unit mass at the start of the radial phase is the same across the whole range of devices [61]. Thus *T*1 with a big *RD* drops the current a lot and strongly depletes the magnetic energy per unit mass at the end of the RD, leading to a small *ED*. Consequently *T*1 are completely fitted using a model that computes only the *RD*, stretching the model parameters until the large *RD* covers also the small *ED*. Conversely a *T*2 PF has a small *RD*, consequently a large *ED* and cannot be completely fitted with the computed *RD*. Thus a big RD drops the current a lot and strongly depletes the magnetic energy per unit mass at the end of the REGULAR radial phase. Hence a device with small RL produces a big RD and ends up with relatively less energy per unit mass at the end of the REGULAR phase when compared to a device with a big value of R_L. Therefore a big *RD* generally tends to lead to a small *ED*; whereas a small *RD* is more conducive to lead to a larger *ED*.

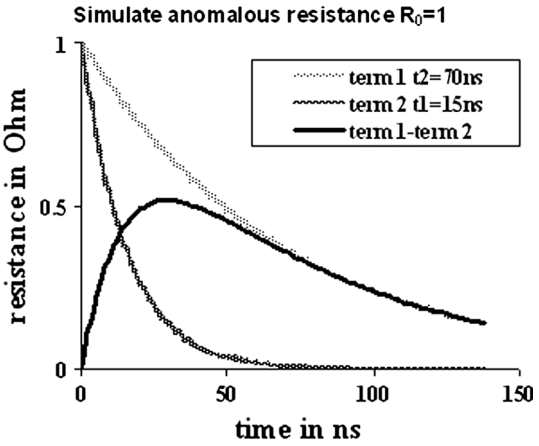

Fig. 8 Simulating anomalous resistance. Term 1 and term 2 refer to the two terms on the right hand side of Eq. (56)

Table 1 Anomalous resistances used for the fitting

ED	R_0 (Ω)	t_2 (ns)	t_1 (ns)	*Endfraction*
Dip 1	1.0	70	15	0.53
Dip 2	0.2	70	40	0.4
Dip 3	0.5	70	25	1.0

From the above we summarised that T1 PF has a big *RD*, consequently a small *ED* and hence can be completely fitted using a model that computes only the *RD*, which is able to stretch its *RD* by stretching the model parameters until the large *RD* covers also the small *ED*. Moreover energetically and mass-wise the fitting is correct. On the other hand *T*2 PF has a small *RD*, consequently a large *ED*. *T*2 PF cannot be completely fitted with the *RD* computed from the code, no matter how the model parameters are stretched. To fit the computed current trace to the measured current for *T*2, a phase 4a needs to be included into the model in order to progress the current dip beyond the small *RD* into the large *ED* part of the current dip.

One way to simulate the current *ED* is to assign the phase 4a period with an anomalous resistance term such as:

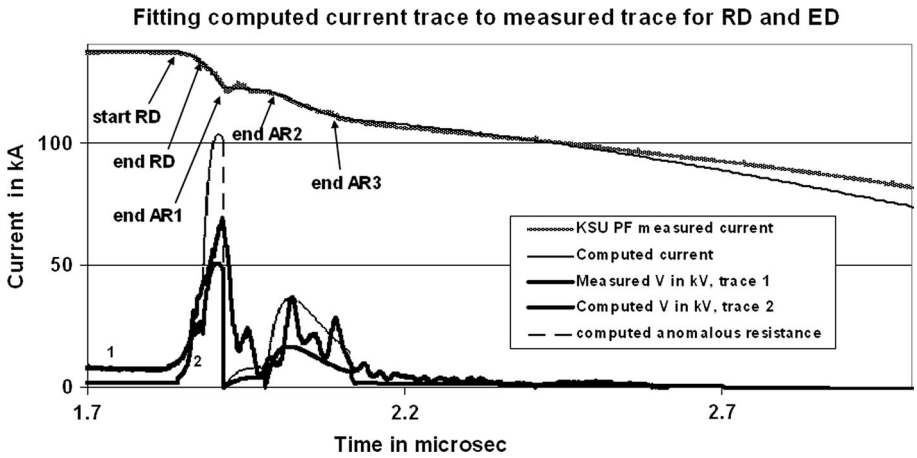

Fig. 9 Computed current (dip region only and expanded to see details) fitted to measured current with inclusion of Phase 4a. Note that the computed current trace is fitted so well to the measured current trace that the two traces lie very closely on top of each other, these being the topmost traces (overlapping). Note also that the computed trace is stopped at 2.6 μs which is beyond the end of the AR3

$$R = R_0[\exp(-t/t_2) - \exp(-t/t_1)] \quad (56)$$

where R_0 could be of the order of 1 Ω, t_1 is a characteristic time representative of the rise time of the anomalous resistance and t_2 is characteristic of the fall time of the anomalous resistance (Fig. 8).

We have applied this technique to the KSU current waveform (Fig. 7). We note that using the 5-phase code, the computed *RD* does not follow the measured current dip which goes on to an *ED*. Following that first current dip in this particular case the dip continues in a second portion which is almost flat then followed by a third section which is less steep than the first dip but of slightly longer duration. We applied a resistance term to each of the three sections. We adjusted the parameters R_0, t_2 and t_1 for each of the section as well as a fraction (*endfraction*) which terminates the term. The fitted parameters are as follows (Table 1).

With these parameters it is found that the computed current dip now fits the measured current dip all the way to the end of the current dip at 2.1 μs (See Fig. 9) and even beyond to 2.6 μs where the computation ends as we are not interested in the fitting beyond phase 4a. The fitting involved the fitting of the *RD* followed by the *ED* of the first dip, then the second and third dips treated as *ED*'s each requiring a separate anomalous resistance function of the type Eq. (56).

The resistance functions used for the fitting are also shown in Fig. 9 (dashed trace, with the resistance values magnified 200 times in order to be visible on the scale of Fig. 9). The computed voltage waveform is also shown (trace labeled 2) compared with the measured voltage waveform (trace labeled 1). The correspondence of the computed voltage waveform and the measured is seen clearly. The lower measured values of voltage may be attributed to the inadequate frequency response of the resistive divider voltage probe.

Conclusion

This paper presents for the first time the complete 5-phase Lee model code, which is found to be adequate for fitting the computed current waveform and the measured waveform of each low L_0 (Type 1) PF by varying two pairs of mass and current factors, one each for the axial and radial phases. Once fitted the code outputs in tabular and graphical forms realistic axial and radial dynamics (positions and speeds), pinch length and minimum pinch radius, temperatures and densities, Bremsstrahlung and line yields, thermonuclear and beam-target line yields, fast ion beam flux and fluence, energy flux and fluence, power flow and damage factors, fast plasma stream energies and speeds. All tests to date of computed with measured quantities have shown good agreement. The paper also reviews the considerable results of the code of designing and optimizing machines, providing expected neutron, soft X-rays (various gases) and ion beams (various gases) yields, giving insights into current and neutron yield limitations, deterioration of neutron scaling (neutron saturation), radiative collapse, speed-enhanced PF, current-stepped PF and extraction of diagnostic data and anomalous resistance data from current signals. Yield scaling laws for neutron, soft X-rays and ion beams are obtained from the code. In one respect the 5-phase code has been found wanting. For high L_0 (Type 2) PF devices it is able to fit the computed current trace to the first part of the measured current trace; but the measured current then exhibits a much larger 'extended' dip which the computed current cannot be fitted; although the 5-phase code does produce reasonable values of neutron and SXR yields in comparison with measured yields even for the high L_0 cases. The paper concludes with an extended 6-phase code in order to complete the current fitting for high L_0 machines. An important use of the 6-phase code is for gathering data on the anomalous resistance of the PF.

Acknowledgments The author acknowledges students, colleagues and collaborators who have in one way or another contributed to the development of this code over the past 3 decades.

References

1. N.V. Filippov, T.I. Filippova, V.P. Vinogradov, Nucl. Fusion. Suppl 2, 577 (1962). http://www.osti.gov/energycitations/product.biblio.jsp?osti_id=4731683
2. J.W. Mather, Phys. Fluids **7**, S28 (1964)
3. D.E. Potter, Phys. Fluids **14**, 1911 (1971)
4. M. Trunk, Plasma Phys. **17**, 237–248 (1975)
5. A. Bernard et al., J. Moscow Phys. Soc. **8**, 93–170 (1998). http://www.icdmp.pl/pf1000.html
6. M. Krishnan, IEEE Trans. Plasma Sci. **40**(12), 3189–3221 (2012)
7. S. Lee, T.Y. Tou, S.P. Moo, M.A. Eissa, A.V. Gholap, K.H. Kwek, S. Mulyodrono, A.J. Smith, S. Suryadi, W. Usada, M. Zakaullah, Am. J. Phys. **56**, 62 (1988)
8. S. Lee, *Twelve Years of UNU/ICTP PFF: A Review IC, 98 (231) Abdus Salam ICTP, Miramare, Trieste*, (ICTP OAA, 1998), http://eprints.ictp.it/31/
9. S. Lee, C.S. Wong, Initiating and strengthening plasma research in developing countries. Phys.Today **59**, 31–36 (2006)
10. S. Lee in *Radiation in Plasmas*, vol II, ed. by B. McNamara. Proceedings of Spring College in Plasma Physics 1983, ICTP, Trieste, (World Scientific Pub Co, Singapore, 1984). ISBN 9971-966-37-9, p. 978–987
11. S. Lee, B.C. Tan, C.S. Wong, A.C. Chew (eds.), *Laser and Plasma Technology*. Proceedings of First Tropical College on Applied Physics 26th Dec 1983–14th Jan 1984, (World Scientific Publishing Co., Kuala Lumpur, 1985). ISBN 9971-978-27-X, p. 38–62
12. S. Lee, *Radiative Dense Plasma Focus Computation Package: RADPF* (2014). http://www.plasmafocus.net; http://www.intimal.edu.my/school/fas/UFLF/ (archival websites)
13. T.Y. Tou, S. Lee, K.H. Kwek, IEEE Trans. Plasma Sci. **17**, 311–315 (1989)
14. S.P. Moo, C.K. Chakrabarty, S. Lee, IEEE Trans. Plasma Sci. **19**, 515–519 (1991)
15. D.E. Potter, Nucl. Fusion **18**, 813–823 (1978)
16. A. Serban, S. Lee, Plasma Sources Sci. Technol. **6**, 78 (1997)
17. M.H. Liu, X.P. Feng, S.V. Springham, S. Lee, IEEE Trans. Plasma Sci. **26**, 135 (1998)
18. S. Lee, P. Lee, G. Zhang, X. Feng, V.A. Gribkov, M. Liu, A. Serban, T. Wong, IEEE Trans. Plasma Sci. **26**, 1119 (1998)
19. S. Lee, (2013), http://ckplee.home.nie.edu.sg/plasmaphysics/ (archival website)
20. D. Wong, P. Lee, T. Zhang, A. Patran, T.L. Tan, R.S. Rawat, S. Lee, Plasma Sources Sci. Technol. **16**, 116 (2007)
21. V. Siahpoush, M.A. Tafreshi, S. Sobhanian, S. Khorram, Plasma Phys. Control. Fusion **47**, 1065 (2005)
22. L. Soto, P. Silva, J. Moreno, G. Silvester, M. Zambra, C. Pavez, L. Altamirano, H. Bruzzone, M. Barbaglia, Y. Sidelnikov, W. Kies, Braz. J. Phys. **34**, 1814 (2004)
23. H. Acuna, F. Castillo, J. Herrera, A. Postal, Int. Conf. Plasma Sci. (1996), Conf. Record, p. 127
24. C. Moreno, V. Raspa, L. Sigaut, R. Vieytes, Appl. Phys. Lett. **89**, 091502 (2006)
25. A.E. Abdou, M.I. Ismail, A.E. Mohamed, S. Lee, S.H. Saw, R. Verma, IEEE Trans. Plasma Sci. **40**(10), 2741–2744 (2012). doi:10.1109/TPS.2012.2209682
26. S. Lee, A sequential plasma focus. IEEE Trans. Plasma Sci. **19**, 912–919 (1991)
27. S.H. Saw, M. Akel, P.C.K. Lee, S.T. Ong, S.N. Mohamad, F.D. Ismail, N.D. Nawi, K. Devi, R.M. Sabri, A.H. Bajian, J. Ali, S. Lee, J. Fusion Energ. **31**, 411–417 (2012). doi:10.1007/s10894-011-9487-z
28. S.H. Saw, P.C.K. Lee, R.S. Rawat, S. Lee, IEEE Trans. Plasma Sci. **37**, 1276–1282 (2009)
29. S. Lee, R.S. Rawat, P. Lee, S.H. Saw, J. Appl. Phys. **106**, 023309 (2009)
30. S.H. Saw, S. Lee, Energ. Power Eng. **2**(1), 65–72 (2010)
31. M. Akel, S. Al-Hawat, S.H. Saw, S. Lee, J. Fusion Energ. **29**(3), 223–231 (2010)
32. M. Akel, S. Lee, S.H. Saw, IEEE Trans. Plasma Sci. **40**, 3290–3297 (2012)
33. S. Lee, S.H. Saw, R.S. Rawat, P. Lee, A. Talebitaher, A.E. Abdou, P.L. Chong, F. Roy, A. Singh, D. Wong, K. Devi, IEEE Trans. Plasma Sci. **39**, 3196–3202 (2011)
34. S. Lee, S.H. Saw, J. Fusion Energ. **27**, 292–295 (2008)
35. S. Lee, S.H. Saw, L. Soto, S.V. Springham, S.P. Moo, Plasma Phys. Control. Fusion **51**, 075006 (2009)
36. S. Lee, S.H. Saw, Appl. Phys. Lett. **92**, 021503 (2008)
37. S. Lee, P. Lee, S.H. Saw, R.S. Rawat, Plasma Phys. Control. Fusion **50**, 065012 (2008)
38. S. Lee, Plasma Phys. Control. Fusion **50**, 10500 (2008)
39. S. Lee, Appl. Phys. Lett. **95**, 151503 (2009)
40. S. Lee, S.H. Saw, J. Ali, J. Fusion Energ. **32**, 42–49 (2013). doi:10.1007/s10894-012-9522-8
41. S. Lee, S.H. Saw, J. Fusion Energ. **31**, 603–610 (2012). doi:10.1007/s10894-012-9506-8
42. S. Lee, S.H. Saw, P.C.K. Lee, R.S. Rawat, H. Schmidt, Appl. Phys. Lett. **92**, 111501 (2008)
43. S.H. Saw, S. Lee, F. Roy, P.L. Chong, V. Vengadeswaran, A.S.M. Sidik, Y.W. Leong, A. Singh, Rev. Sci. Instrum. **81**, 053505 (2010)
44. S. Lee, S.H. Saw, R.S. Rawat, P. Lee, R. Verma, A. Talebitaher, S.M. Hassan, A.E. Abdou, M. Ismail, A. Mohamed, H. Torreblanca, S. Al Hawat, M. Akel, P.L. Chong, F. Roy, A. Singh, D. Wong, K.K. Devi, J. Fusion Energ. **31**, 198–204 (2012)
45. S. Lee, S.H. Saw, P.C.K. Lee, R.S. Rawat, K. Devi, J. Fusion Energ. **32**, 50–55 (2013). doi:10.1007/s10894-012-9521-9
46. S.H. Saw, R.S. Rawat, P. Lee, A. Talebitaher, A.E. Abdou, P.L. Chong, F. Roy Jr., J. Ali, S. Lee, SXR measurements in INTI PF operated in neon to identify typical (Normal N) profile for shots with good yield. IEEE Trans. Plasma Sci. **41**(11), 3166–3172, (2013), ISSN 0093-3813. doi:10.1109/TPS.2013.2281333
47. S. Lee, S.H. Saw, A.E. Abdou, H. Torreblanca, J. Fusion Energ. **30**, 277–282 (2011)
48. R.A. Behbahani, F.M. Aghamir, J. Appl. Phys. **111**(4), 043304–043305 (2012)
49. R.A. Behbahani, F.M. Aghamir, Phys. Plasmas **18**, 103302 (2011). doi:10.1063/1.3647958
50. S. Lee, S.H. Saw, Phys. Plasmas **19**, 12703 (2012). doi:10.1063/1.4766744
51. S. Lee, S.H. Saw, Phys. Plasmas **20**, 062702 (2013). doi:10.1063/1.4811650
52. S. Lee, S.H. Saw, *Special Edition on "Fusion Energy" Energies* 2010, **3**, 711–737 (2010). doi:10.3390/en3040711, Published online 12 April 2010
53. S.H. Saw, S. Lee, Int. J. Energy Res. **35**, 81–88 (2011). doi:10.1002/er.1758
54. S. Lee, S.H. Saw, Int. J. Energ. Res. **36**(15), 1366–1374 (2012)
55. S. Lee, S.H. Saw, P. Lee, R.S. Rawat, Plasma Phys. Control. Fusion **51**, 105013 (2009)
56. S.P. Chow, S. Lee, B.C. Tan, J. Plasma Phys. **8**, 21–31 (1972)
57. S. Al-Hawat, M. Akel, S.H. Saw, S. Lee, J. Fusion Energ. **31**, 13–20 (2012)

58. S. Lee, S.H. Saw, H. Hegazy, J. Ali, V. Damideh, N. Fatis, H. Kariri, A. Khubrani, A. Mahasi, J. Fusion Energ. (2014). doi:10.1007/s10894-013-9658-1
59. S. Lee, Aust. J. Phys. **3**, 891–895 (1983)
60. P.L. Chong, S. Lee, S.H. Saw, J. Eng. Sci. Technol. **8**(1), 27–33 (2013)
61. S. Lee, A. Serban, IEEE Trans. Plasma Sci. **24**, 1101–1105 (1996)
62. www.plasmafocus.net/IPFS/modelpackage/Corona%20Calculations/C1coronaIntroduction.htm
63. L. Spitzer, Physics of fully ionised gases, in *Interscience Tracts on Physics and Astronomy*, 2nd rev. (Interscience Publication, New York, 1965)
64. J.W. Shearer, Phys. Fluids **19**, 1426 (1976). doi:10.1063/1.861627
65. R. Pease, Proc. Phys. Soc. **70**, 11 (1957)
66. S. Braginskii, Zh. Eksp. Teor. Fiz. **33**, 645 (1957)
67. K. Koshelev, N. Pereira, J. Appl. Phys. **69**, 21–44 (1991)
68. A.E. Robson, Phys. Fluid **B3**, 1481 (1991)
69. N.A.D. Khattak, *Anomalous Heating (LHDI)* (2011). http://www.plasmafocus.net/IPFS/modelpackage/File3Appendix.pdf
70. J.D. Huba, *2006 Plasma Formulary pg44*. http://wwwppd.nrl.navy.mil/nrlformulary/NRL_FORMULARY_07.pdf
71. V.A. Gribkov, A. Banaszak, B. Bienkowska, A.V. Dubrovsky, I. Ivanova-Stanik, L. Jakubowski, L. Karpinski, R.A. Miklaszewski, M. Paduch, M.J. Sadowski, M. Scholz, A. Szydlowski, K. Tomaszewski, J. Phys. D Appl. Phys. **40**, 3592–3607 (2007)
72. S.V. Springham et al., Nukleonika **51**(1), 47–53 (2006)
73. S.V. Springham, S. Lee, M.S. Rafique, Plasma Phys. Control. Fusion **42**(10), 1023 (2000)
74. W. Kies in *Laser and Plasma Technology*, ed. by S. Lee, B.C. Tan, C.S. Wong, A.C. Chew, K.S. Low, H. Ahmad, Y.H. Chen, Proceedings of Second Tropical College (World Scientific, Singapore, 1988). ISBN 9971-50-767-6, p. 86–137
75. H. Herold in *Laser and Plasma Technology*, ed. by C.S. Wong, S. Lee, B.C. Tan, A.C. Chew, K.S. Low, S.P. Moo, Proceedings of Third Tropical College (World Scientific, Singapore, 1990). ISBN 981-02-0168-0, p. 21–45
76. A. Patran, R.S. Rawat, J.M. Koh, S.V. Springham, T.L. Tan, P. Lee, S. Lee, *31st EPS Conference on Plasma Phys. London*, 2004 ECA vol **28G**, P-4.213 (2004)
77. R. Verma, M.V. Roshan, F. Malik, P. Lee, S. Lee, S.V. Springham, T.L. Tan, M. Krishnan, Plasma Sources Sci. Technol. **17**(4), 045020 (2008)
78. V. Rishi, R.S. Rawat, P. Lee, S. Lee, S.V. Springham, T.L. Tan, M. Krishnan, Phys. Lett. A **373**, 2568–2571 (2009)
79. M. Favre, S. Lee, S.P. Moo, C.S. Wong, Plasma Sources Sci. Technol. **1**(2), 122 (1992)
80. S.L. Yap, S.H. Lee, L.K. Lim, C.S. Wong, in *Proceedings International Workshop on Plasma Computations and Applications (IWPCA2008)*, ed. by S.H. Saw et al. (INTI Publishing House Sdn Bhd, Malaysia, 2008). ISSN 165-0284, p. 51–54